Validation of the Corcos Model for the Space Launch System using Unsteady Pressure Sensitive Paint

Francesco Soranna*, Patrick S. Heaney†, Martin K. Sekula‡, David J. Piatak§, and James M. Ramey¶
NASA Langley Research Center, Hampton, VA 23681

During atmospheric ascent, launch vehicles (LVs) experience large dynamic loads at transonic conditions where aerodynamic buffet is most critical. To estimate buffet loads, coupled loads analyses typically utilize suitable forcing functions, called buffet forcing functions (BFFs). One of the key buffet environment contributors is the turbulent boundary layer (TBL) on the LV outer skin. The TBL-induced fluctuating pressures can be estimated using the widely-accepted Corcos model. In the context of transonic buffet, the performance of this model is not well established, partly because of lack of data. To fill this gap, NASA recently acquired extremely high-spatial-density data for the Space Launch System (SLS) vehicle, using the unsteady pressure sensitive paint (uPSP) optical measurement technique. A methodology is developed for validation of the Corcos model using these unique data, with a focus on the LV-design application. The model hypotheses are verified and the model parameters are empirically tuned. For selected panels on the vehicle, BFF coherence factors are derived based on the Corcos model and the associated panel BFFs are compared to uPSP data. It is shown that the modeled BFFs are in agreement with direct integration of uPSP data, except for regions where pressure fluctuations are spatially nonuniform. In those regions, the Corcos-based BFFs exhibit inherent limitations of BFF estimation methods that rely on discrete pressure measurements.

Notice to Readers

The Space Launch System, including its predicted performance and certain other features and characteristics, have been defined by the U.S. Government to be Controlled Unclassified Information (CUI). Information deemed to be CUI requires special protection and may not be disclosed to an international audience. To comply with CUI restrictions, details such as absolute values have been removed from some plots and figures in this paper. It is the opinion of the authors that despite these alterations, there is no loss of meaningful technical content. Analytical methodologies and capabilities are discussed, significant and interesting technical results are still present, and meaningful conclusions are presented.

Acronyms

ATAT	=	Ascent Transient Aerodynamics Test
BFF	=	Buffet Forcing Function
CLA	=	Coupled Loads Analyses
FAH	=	Forward Attachment Hardware
FRF	=	Frequency Response Function
LV	=	Launch Vehicle
OML	=	Outer Mold Line
SLS	=	Space Launch System
TBL	=	Turbulent Boundary Layer
uPSP	=	Unsteady Pressure Sensitive Paint

*Research Aerospace Engineer, Aeroelasticity Branch, AIAA Member
†Research Aerospace Engineer, Aeroelasticity Branch, AIAA Member
‡Senior Research Aerospace Engineer, Aeroelasticity Branch
§Assistant Branch Head, Aeroelasticity Branch, AIAA Senior Member
¶Research Aerospace Engineer, Aeroelasticity Branch, AIAA Member

Nomenclature

A, B	=	streamwise and crossflow coherence functions
A_z	=	projected area of panel in the z-direction
$\Delta C_{p,\text{rms}}$	=	root-mean-square of pressure coefficient (mean removed)
D	=	core diameter
F_i	=	panel orthogonal buffet forcing function, acting in the i-direction ($i = x, y, z$)
$\widetilde{F_i}$	=	panel fully-coherent buffet forcing function
F_s	=	sampling rate
$\mathcal{F}$	=	Fourier transform
H	=	frequency response function
i	=	axis indices, frequency index
j, k	=	supernode indices
l_i	=	coherence length along the longitudinal ($i = 1$) or azimuthal ($i = 3$) directions
L	=	longitudinal width of panel
N	=	number of uPSP samples
S	=	arclength of panel
t	=	time
Q	=	freestream dynamic pressure
x, y, z	=	longitudinal, lateral, and vertical axes of the vehicle
U_c	=	turbulence-convection velocity
α_1, α_3	=	streamwise and crossflow decay constants
α	=	angle-of-attack
β	=	sideslip angle
Γ	=	cross-spectral density function
γ	=	coherence function
θ	=	body coordinate system azimuthal angle
$\boldsymbol{\xi}$	=	measurement separation vector
ξ_1, ξ_3	=	streamwise and crossflow separation vector components
ϕ	=	autospectrum
Φ_i^F	=	power spectral density of the force F_i
ω	=	angular frequency
ω_1	=	lower bound angular frequency of low-frequency bin
ζ	=	coherence factor
ζ_i	=	coherence factors along the longitudinal ($i = 1$) or azimuthal ($i = 3$) directions

I. Background and Methodology

In the design of launch vehicles (LVs), special attention is given to transonic buffet loads, often ranking among the highest dynamic loads predicted by coupled loads analyses (CLA, Ref. [1]). To model these buffet loads, CLA employs suitable forcing functions, called buffet forcing functions (BFFs) [2] that consist of unsteady loads in the time or frequency domain at many discrete locations on the LV. The BFFs model various aerodynamic environments associated with buffet, including: turbulent boundary layers (TBLs), shocks, flow separation, protuberance wake, etc.

A great amount of effort is involved in LV BFF estimation. The state-of-the-art approach to developing these BFFs consists of transonic wind-tunnel tests where a rigid buffet model of an LV is instrumented with hundreds of pressure transducers that measure pressure fluctuations at discrete locations on the surface of the model. These pressures are then integrated across the surface of the LV and coherence factors are applied to account for the pressure spatiotemporal variation ignored in the pressure integration process (Refs.[3–5]).

The computation of coherence factors requires knowledge of the cross-spectral density, Γ, between surface pressures at different points on the LV. For a new LV design, where data are lacking, or when the spatial resolution of the pressure measurements is insufficient, aerodynamicists need to rely on analytical methods to estimate Γ. Often the focus is on modeling the wall pressure fluctuations caused by TBLs, and the Corcos model [6] provides a relatively simple tool to estimate Γ.

This paper focuses on validation of the Corcos model for the Space Launch System (SLS) LV. First, the model hypotheses are verified against high-spatial-resolution data from unsteady pressure sensitive paint (uPSP) measurements on the SLS Block 1 cargo configuration provided in Fig. 1. Next, for selected regions of the vehicle, the model parameters are calibrated over a range of Mach numbers and attitude conditions. Finally, coherence factors are estimated using the calibrated Corcos model and compared to coherence factors obtained by direct integration of uPSP data. Sample panel BFFs are computed from the modeled coherence factors and analyzed against uPSP-based panel BFFs.

A. Test description

The data were collected during the SLS Ascent Transient Aerodynamics Test (ATAT) conducted in August and September 2019 at the NASA Ames Research Center (ARC) Unitary Plan Wind Tunnel (UPWT). While ATAT utilized both the 11-Foot Transonic Wind Tunnel (11-Foot TWT) and the 9- by 7-Foot Supersonic Wind Tunnel (9x7 SWT) at UPWT, uPSP data were only collected in the 11-Foot TWT. Using this experimental method, the buffet environments for two SLS configurations were examined: 1) the SLS Block 1 cargo, on which the Europa Clipper Science Mission 1 (SM-1) was initially manifested, and 2) the SLS Block 1B cargo with a low-fineness-ratio ogive payload fairing. The analysis presented in this paper is based on the first configuration, the 2.5-percent scale SLS Block 1 cargo vehicle, shown in Fig. 1. Testing was conducted at a Reynolds number of 3×10^6 per foot, the Mach number ranged between 0.70 and 1.40, and the angle-of-attack and sideslip angles ranged between ±6 degrees. The uPSP measurement technique was utilized to acquire extremely high-spatial-density unsteady-pressure data at a sampling rate of 10 kHz. Details of this optical measurement method are documented in Ref. [7].

B. Methodology

The aforementioned uPSP data were analyzed using a panel method described in Ref. [8]. This method consists of defining contiguous panels on the model surface and spatially averaging the uPSP-measured unsteady pressures over hundreds of uPSP measurement locations within each panel.

The analysis presented next focuses on the SLS Block 1 cargo payload fairing and core stage and ignores the right and left boosters. The ATAT model grid contains 954,894 uPSP nodes of which 479,079 uPSP nodes are located on the core stage. The nodes on the core stage were parsed through 10,800 panels defined by 180 uniformly-spaced longitudinal stations, divided into 60 evenly-spaced azimuthal stations. The corresponding nondimensional longitudinal and azimuthal resolutions are $\Delta x/D = 5.7\%$ and $\Delta\theta/2\pi = 1.7\%$, where x is the longitudinal axis, θ is the body coordinate system azimuthal angle, and D is the core stage diameter. The panel method generates a coarse grid of "supernodes" whose centroids are shown in Fig. 2. In the rest of the paper, the term supernodes will be used.

C. Model formulation

Following the formulation of Refs. [9, 10], the cross-spectral density function $\Gamma(\boldsymbol{\xi}, \omega)$ proposed by Corcos is:

$$\Gamma(\boldsymbol{\xi}, \omega) = \phi(\omega) A(\xi_1 \omega/U_c) B(\xi_3 \omega/U_c) e^{i(\omega \xi_1/U_c)} \tag{1}$$

$$A(\omega\xi_1/U_c) = e^{-\alpha_1 |\omega \xi_1/U_c|} \quad B(\omega\xi_3/U_c) = e^{-\alpha_3 |\omega \xi_3/U_c|} \tag{2}$$

where $\boldsymbol{\xi} = (\xi_1, \xi_3)$ is the separation vector between pressure measurements, and ξ_1 and ξ_3 represent the streamwise and crossflow directions, respectively. The other terms in Eq. 1 are the angular frequency ω, the autospectrum $\phi(\omega) = \Gamma(0, 0, \omega)$, and the turbulence-convection velocity U_c. The quantities α_1 and α_3 (Eq. 2) represent decay constants that typically range between 0.11-0.12 and 0.7-1.2, respectively, for a smooth rigid wall [9]. It is worth highlighting that the Corcos model is based on two hypotheses [10]: 1) a multiplication hypothesis assumes that Γ is a product of simpler functions $A(\xi_1, \omega)$ and $B(\xi_3, \omega)$ (Eq. 1), and 2) a similarity hypothesis such that $A(\xi_1, \omega) = A(\xi_1 \omega/U_c)$ and $B(\xi_3, \omega) = B(\xi_3 \omega/U_c)$.

An important quantity readily derived from Eq. 1 is the coherence function γ, that for homogeneous flow is:

$$\gamma(\boldsymbol{\xi}, \omega) = \left|\Gamma(\boldsymbol{\xi}, \omega)\right| / \phi(\omega) = A(\xi_1, \omega) B(\xi_3, \omega) \tag{3}$$

from which A and B represent the streamwise and crossflow coherence functions, respectively [10]:

$$A(\xi_1, \omega) = \left|\Gamma(\xi_1, 0, \omega)\right| / \phi(\omega) \tag{4}$$

$$B(\xi_3, \omega) = \left|\Gamma(0, \xi_3, \omega)\right| / \phi(\omega) \tag{5}$$

II. Results

To compare the uPSP data to the Corcos model, the coherence function between unsteady pressures at supernodes j and k is computed as:

$$\gamma(\omega) = \frac{\left|\Gamma_{jk}(\omega)\right|}{\sqrt{\phi_j(\omega)\,\phi_k(\omega)}} \tag{6}$$

where Γ_{jk} and $\phi_{j,k}$ are discrete counterparts of the corresponding terms in Eq. 3. Note that for homogeneous flow, $\phi_j = \phi_k = \phi$ and Eq. 6 becomes identical to Eq. 3. Equation 6 is evaluated using the MSCOHERE function in MATLAB™ (since MSCOHERE computes the magnitude-squared-coherence γ^2; here, the square root of the output is used), where the pressure time histories have been windowed using a 512-sample Hamming window with 50% overlap between windows.

In the next sections, the Corcos similarity hypothesis is verified for the longitudinal (i.e., streamwise) and azimuthal (i.e., crossflow) coherence functions. Subsequently, the empirically-derived decay constants α_1 and α_3 (Eq. 2) are used to verify the Corcos multiplication hypothesis.

A. Verification

1. The similarity hypothesis

Longitudinal coherence The most severe buffet-environment on the SLS vehicle is located downstream of the Forward Attachment Hardware (FAH) that connects the solid rocket boosters (SRBs) to the core stage (Fig. 3). Highly-coherent vortex shedding off the FAH results in propagation of vortices down the length of the vehicle, causing significant pressure fluctuations on the SRBs and on the core. Figure 4 presents a distribution of longitudinal coherence $\gamma(\xi_1, 0, \omega)$ over a sample longitudinal segment extending ±1 core diameters from a supernode in proximity to the Block 1 cargo booster FAH. The location of the sample segment is shown on the outer mold line at the bottom of Fig. 4, along with the centroid of the reference supernode. The normalized distance ξ_1/D is measured from the centroid of the supernode. The Mach number is 0.79 and the vehicle is at zero degrees attitude. The highest coherence levels occur within a narrow frequency band that corresponds to one-half the FAH vortex-shedding frequency. Both the FAH vortex-shedding frequency and the FAH vortex-shedding subharmonic are marked in Fig. 4). Spurious wind-tunnel tones contribute to elevated coherence levels in certain frequency bands that are marked in Fig. 4. Away from wind-tunnel generated tones and from frequencies related to FAH vortex-shedding, γ decays with ξ_1 and ω, as expected.

As a preliminary step toward verifying the similarity hypothesis, it is worth taking a closer look at the distribution of $\gamma(\xi_1, 0, \omega)$. Figure 5, on the left column, shows curves of $\gamma(\xi_1)$ corresponding to ω_i = constant slices ($i \in [1, 26]$) of the contour plot of Fig. 4 (the sample ω_i values are marked on the ω-axis in Fig. 4). Note that these ω_i slices avoid non-TBL related frequencies, namely FAH vortex-shedding and tunnel-slot-tone frequencies (Fig. 4). The data shown in Fig. 5 are divided in three frequency bins, corresponding to low-, mid-, and high-frequency ranges (the boundaries of these frequency ranges are marked in Fig. 4). Since coherence lengths decrease with frequency, the decay rate of $\gamma(\xi_1)$ increases with ω, producing a distribution of $\gamma(\xi_1)$ presented in Fig. 5 (left column).

Following Ref. [11], the data shown on the left column of Fig. 5 are plotted on the right column as a function of the similarity variable $\xi_1\omega/U_c$, where the turbulence-convection velocity U_c is assumed equal to half the freestream velocity [8]. Also shown in the right column plots are the Corcos model exponential functions $A(\omega\xi_1/U_c)$ (dashed line in Fig. 5; defined in Eq. 2) for each streamwise decay constant α_1 computed for the appropriate frequency bin. These α_1 constants are listed in Table 1 and discussed further below. It should be noted that assuming constant U_c for regions of the LV where the flow is nonuniform is an open issue that could be addressed in the future. Frequency binning was found to reduce the dependence of $\gamma(\xi_1\omega/U_c)$ on ω within each frequency bin, compared to distributions of $\gamma(\xi_1\omega/U_c)$ obtained by applying Corcos frequency normalization over the full spectrum.

Comparing the left column plots of Fig. 5 to the plots on the right column, Corcos similarity variable $\xi_1\omega/U_c$ produces a reasonable collapse of the $\gamma(\xi_1)$ curves, especially at low and high frequencies. This result is consistent with findings by Ref. [11], who first verified the similarity hypothesis in the context of compressible TBLs, for Mach number ranging from 2 to 4. In the midfrequency range (Fig. 5-b), the $\gamma(\xi_1\omega/U_c)$ data (Fig. 5-b, right column) show an oscillatory behavior, with a secondary peak as high as $\gamma = 0.55$. The same peak can be traced in the contour plot of Fig. 4, see red-dashed line. Such behavior can be modeled using a modified form of the streamwise coherence function:

$$A(\omega\xi_1/U_c) = e^{-\alpha_1\left|\omega\xi_1/U_c\right|}\,\left|\cos(\omega\xi_1/U_c)\right| \,. \tag{7}$$

Note that the expression above corresponds to taking the real part of Eq. 1 and substituting it into the right-hand side of Eq. 4. An expression closely related to Eq. 7 can be found also in Ref. [12].

Figure 6 compares the same $\gamma(\xi_1\omega/U_c)$ data of Fig. 5-b (right column) to the Corcos-modified streamwise coherence function. The latter is obtained by fitting the right-hand side of Eq. 7 through the frequency-normalized distributions $\gamma(\xi_1\omega/U_c > 0)$ shown in Fig. 5-b (right column), which yields a new value of the streamwise decay constant, $\alpha_1 = 0.33$ (compared to 0.78 for the unmodified Corcos model, see Table 1, Mach=0.79, midfrequency range). Comparing the modified Corcos model to uPSP data, Fig. 6 shows good agreement. Although the remainder of the paper focuses on the original formulation of the Corcos coherence functions (Eq. 2), the modified version could be used in the future to improve legacy methods for estimation of coherence factors.

Azimuthal coherence Figure 7 shows contours of $\gamma(0, \xi_3, \omega)$ for the reference supernode of Fig. 4, where ξ_3 represents an arc length measured on the core from the reference supernode, increasing toward the left solid rocket booster, labeled "LSRB" (the ξ_3-axis is marked on the OML at the bottom of Fig. 4). Constant ω slices of $\gamma(0, \xi_3, \omega)$, shown in Fig. 8 on the left column, highlight a spread in the $\gamma(\xi_3)$ data over different frequencies. Similar to $\gamma(\xi_1)$, the $\gamma(\xi_3)$ distributions tend to collapse to a single decaying-exponential function when the data are plotted as a function of the similarity variable $\xi_3\omega/U_c$, as shown on the right column of Fig. 8. Note that frequency binning is applied over the same frequency ranges as shown in Fig. 4. In this case, no oscillatory behavior is observed in the distributions of $\gamma(\xi_3\omega/U_c)$.

Corcos model parameters Table 1 presents values of Corcos decay constants α_1 and α_3 (Eq. 2) for different Mach numbers. These decay constants are obtained by fitting exponential functions through frequency-normalized distributions of $\gamma(\omega\xi_i/U_c > 0)$ (i=1,3) obtained using uPSP data, such as those shown for Mach=0.79 in Figs. 5 and 8 (right columns). Curve fitting is done for each frequency bin independently, thus yielding a set of decay constants (α_1,α_3) for each frequency bin.

Focusing first on the Mach=0.79 condition, the dashed curves in Figs. 5 and 8 (right columns) show the Corcos functions $A(\omega\xi_1/U_c)$ and $B(\omega\xi_3/U_c)$ (Eq. 2) corresponding to each set (α_1,α_3) listed in the first 3 rows of Table 1. For this condition (Mach=0.79), Table 1 shows that the low-frequency range is characterized by higher coherence-decay rates compared to the mid- and high-frequency counterparts. Also, α_1 is greater than the typical incompressible TBL value of 0.11-0.12, while α_3 is within the incompressible TBL range of 0.7-1.2 (for the mid- and high-frequency ranges).

To elucidate trends from Table 1, Fig. 9 shows plots of the Corcos model decay constants as a function of Mach number. As a reference, the incompressible TBL values mentioned in the last paragraph are shown by dashed lines. In the mid- and high-frequency ranges, α_1 and α_3 share similar trends with Mach number. The low-frequency distributions of both decay constants stand out, especially α_1, which follows a monotonically increasing trend with Mach number. A point worth highlighting is that, for the conditions analyzed, both α_1 and α_3 show distinct changes near Mach=0.91. Focusing on α_1 (Fig. 9-a), in the low-frequency range, its distribution has an inflection near Mach=0.91. Near the same Mach number, the mid- and low-frequency-range profiles of α_1 have local minima. Regarding α_3 (Fig. 9-b), local minima exist near Mach=0.91 for each frequency bin. Certain consequences of these distinct changes near Mach=0.91 will be discussed later in the paper.

Once a set of decay constants is determined for a given frequency range, the Corcos model can be used to estimate $\gamma(\xi_i)$ for any specific frequency within its applicable range. This estimation simplifies bookkeeping the decay constants for each frequency of interest. Figure 10 shows a posteriori test of the Corcos model for Mach=0.79, choosing a sample ω in the low-frequency range, using the constants from Table 1. In this case, the Corcos model (black line) is in good agreement with the uPSP-based data (blue symbols). Some discrepancies are found at very low frequency and, as expected, in the mid-frequency range (not presented). In the latter case, the discrepancies are due to the previously-described oscillatory behavior of the streamwise coherence function (Fig. 6).

2. The multiplication hypothesis

Recall that Corcos multiplication hypothesis assumes γ is the product of the streamwise and crossflow coherence functions (see Eq. 3). To verify this hypothesis, an approach similar to one used by Singer [10] is used. The left hand side of Eq. 3, based on uPSP data, is compared to the right hand side, where A and B are based on Corcos exponential functions (Eq. 2).

Figure 11 presents contours of $\gamma(\xi_1, \xi_3)$ for sample frequencies within the low-, mid-, and high-frequency ranges. The Mach number is 0.79 and the vehicle is at zero degrees attitude. The solid lines, and the associated color intensities,

Table 1 Corcos model decay constants for the sample region on the SLS Block 1 cargo core stage shown in Fig. 4.

Mach	α	β	frequency	α_1	α_3
0.79	0.0	0.0	low	2.22	3.61
			mid	0.78	0.77
			high	0.65	0.54
0.91	0.0	0.0	low	3.02	0.59
			mid	0.24	0.19
			high	0.19	0.41
0.95	-4.0	0.0	low	5.33	1.46
			mid	1.49	1.32
			high	1.31	1.39
1.10	0.0	0.0	low	11.20	2.37
			mid	1.28	0.43
			high	0.45	0.62

are based on uPSP data, and represent the benchmark. The dashed lines show the product A times B (Eq. 3), where the decay constants for the exponential functions (Eq. 2) are based on Table 1. Trends are in general agreement, with comparable contour levels, especially in the $\gamma \sim 0.6 - 1.0$ -range. However, as noted by Singer [10] (and improved upon by his model), the multiplication hypothesis produces straight lines that are in contrast with more elliptical or irregular contour shapes of the benchmark.

B. Coherence lengths

The goal of this section is to establish a way to compare estimated coherence lengths based on the Corcos model to uPSP data. Coherence lengths are closely related to coherence functions through the equation (Ref. [13]):

$$l_i(\omega) = \int_0^\infty \gamma(\omega, \xi_i)\, \mathrm{d}\xi_i \tag{8}$$

for the streamwise ($i = 1$) and crossflow ($i = 3$) directions. Using the Corcos model, substituting the expressions for A and B from Eq. 2 into Eq. 8 yields the Corcos-based coherence lengths:

$$l_i = \frac{U_c}{\alpha_i\, \omega}\ . \tag{9}$$

On the other hand, using uPSP data, the integral in Eq. 8 is computed at each frequency by fitting an exponential function $\gamma(\omega, \xi_i) = e^{-\xi_i\, /\, l_i(\omega)}$ to the experimentally-derived values of γ (Refs.[4, 14]) to yield the uPSP-based coherence lengths.

Figure 12 provides an example of streamwise and crossflow coherence-lengths distributions as a function of ω on a logarithmic scale, as derived from the Corcos model and from uPSP data, for Mach=0.79 and zero degrees attitude. For each frequency bin, the appropriate decay constants listed in Table 1 are substituted into Eq. 9. Coherence lengths estimated based on the Corcos model, by definition, follow a ω^{-1} trend (Eq. 9) and provide a reasonable approximation of those directly computed from the benchmark uPSP data. However, trends of uPSP-based coherence lengths are nonmonotonic, due to the impact that vortex shedding has on the coherence function as well as spurious tunnel tones, such as those marked in Fig. 12.

C. Coherence factors

1. Methodology

The concept of coherence factors is based on the original work by Dahm[15], followed by Piatak et al. [2] and Panda [4]. To explain this concept requires the introduction of certain definitions. Consider a buffet region defined by a panel on the core stage, such as panel #2 shown in Fig. 2, and let $F_z(t)$ be a fluctuating force acting on this panel in the z-direction (the following arguments apply to F_y as well). This fluctuating force is referred to as a Buffet Forcing Function (BFF). If ΔC_p (Δ =mean removed) is the pressure coefficient at a reference supernode inside the panel (marked by a red circle in Fig. 2 inset), a fully-coherent estimate of $F_z(t)$ is:

$$\widetilde{F}_z(t) = \Delta C_p(t)\, Q\, A_z \tag{10}$$

where Q is the freestream dynamic pressure, and A_z is the projected area of the panel in the z-direction. A frequency response function $H(\omega)$ can be defined as:

$$H(\omega) = \frac{F_z(\omega)}{\widetilde{F}_z(\omega)} = \frac{F_z(\omega)}{C_p(\omega)\, Q\, A_z} = \frac{\mathcal{F}(F_z(t))}{\mathcal{F}(C_p(t))\, Q\, A_z} \tag{11}$$

where $F_z(\omega)$, $\widetilde{F}_z(\omega)$, and $C_p(\omega)$ (the symbol Δ has been dropped for simplicity) are Fourier transforms $\mathcal{F}$ from the time to the frequency domain. Note that, by definition, $|H(\omega)| \leq 1$ due to partially correlated fluctuating pressures on any given buffet region (see Ref. [4]).

The goal of BFF estimation methods is to find a suitable approximation of $H(\omega)$ such that F_z can be estimated based on $\widetilde{F}_z$ from Eq. 11, i.e., $F_z(\omega) = H(\omega)\, C_p(\omega)\, Q\, A_z$. A typical assumption is that:

$$|H(\omega)| \sim \zeta(\omega) \tag{12}$$

where $\zeta(\omega)$ is a coherence factor that, in the present work, is defined as follows:

$$\zeta(\omega) = \frac{\zeta_1(\omega) + \zeta_3(\omega)}{2} \tag{13}$$

$$\zeta_1(\omega) = \sqrt{\frac{l_1(\omega)}{L}}\,, \quad \zeta_3(\omega) = \sqrt{\frac{l_3(\omega)}{S}}\,. \tag{14}$$

In Eq. 14, ζ_1 and ζ_3 are streamwise and crossflow coherence factors, l_1 and l_3 represent coherence lengths, L and S represent the longitudinal width and arclength of the reference panel (Fig. 2), respectively. The Corcos-based coherence factors are obtained by substituting $l_1(\omega)$ and $l_3(\omega)$ from Eq. 9 into Eq. 14:

$$\zeta_1(\omega) = \sqrt{\frac{U_c}{\alpha_1\, \omega\, L}}\,, \quad \zeta_3(\omega) = \sqrt{\frac{U_c}{\alpha_3\, \omega\, S}}\,. \tag{15}$$

In the next subsection, ζ_i (i=1,3) based on the Corcos model is computed and compared to $|H(\omega)|$ (Eq. 12) based on uPSP data.

2. Application

Figure 13 shows Corcos-based coherence factors for the sample panel #2 of Fig. 2. Application of Eq. 15 yields coherence factors (ζ_1, ζ_3, ζ) for the low-, mid-, and high-frequency ranges. Note that ζ_i are set constant equal to 1 for frequencies where $l_1(\omega) \geq L$ and $l_3(\omega) \geq S$, i.e., when the streamwise and crossflow coherence lengths exceed the panel's characteristic dimensions. On the other hand, when $l_1(\omega) < L$ and $l_3(\omega) < S$, based on Eq. 15, $\zeta_1(\omega)$ and $\zeta_3(\omega)$ follow a $\omega^{-0.5}$ trend, as shown on logarithmic scale by -0.5 slope linear functions (Fig. 13, blue lines corresponding to ζ_1 and black-dashed lines representing ζ_3). Averaging ζ_1 and ζ_3 (Eq. 13) results in the distributions of $\zeta(\omega)$ that are shown by red-solid lines in Fig.13. To define $\zeta(\omega)$, in alternative to averaging, one could take the product between ζ_1 and ζ_3 (in place of Eq. 13). However, the resulting trend $\zeta \sim \omega^{-1.0}$ leads to excessive BFF attenuation (not shown here for brevity, see discussion in the next section on how coherence factors are utilized for BFF attenuation).

As a benchmark for the Corcos model, Fig. 13 shows the uPSP-based function $|H(\omega)|$, represented by a green curve. According to Eq. 11, $H(\omega)$ was computed from the frequency response function (FRF) between the input signal $\widetilde{F}_z(t)$

(Eq.10) and output signal $F_z(t)$. Specifically, the fully-coherent fluctuating force $\widetilde{F}_z(t)$ is based on C_p measured by a reference uPSP supernode within panel #2, marked in red in the Fig. 2 inset (and in Fig. 4). The benchmark, $F_z(t)$, was calculated through vector summation of the z-component fluctuating forces at each uPSP supernode within panel #2 (Fig. 2). The FRF was obtained by computing the FFT of $\widetilde{F}_z(t)$ and $F_z(t)$ and fitting a 2nd- order polynomial through the ratio $|F_z(\omega)/\widetilde{F}_z(\omega)|$ over the frequency range $\omega \in 2\pi[0, F_s/2]$, where F_s is the uPSP sampling rate, and $F_s/2$ is the Nyquist frequency.

Comparing distributions in Fig. 13, within a typical transonic buffet bandwidth, trends of the Corcos-based coherence factor $\zeta(\omega)$ (red-solid lines) are consistent with $|H(\omega)|$ (green curve). Comparison of coherence factors at higher Mach numbers are shown in Fig. 14 for panel #2. At Mach=0.91 (Fig. 14-a), coherence factors are higher compared to Mach=0.79 (Fig. 13), especially in the mid frequency-range where $\zeta = 1$. At Mach=0.91, both the FAH vortex-shedding frequency and its subharmomic occur within this frequency range. From Table 1, for the midfrequency range, the decay constants α_1 and α_3 at Mach=0.91 are 70-75% lower than their counterparts at Mach=0.79, indicating that pressure fluctuations in this region (panel #2) are significantly more coherent at Mach=0.91 than at lower Mach number, thus resulting in larger values of ζ. Figure 14-b presents coherence factors for a Mach=0.95 condition with the vehicle at $\alpha = -4.0$ deg angle-of-attack. At this vehicle attitude, where panel #2 is on the windward side of the core stage, there is a good agreement between ζ and $|H(\omega)|$. In the next section, these Corcos-based coherence factors are utilized to estimate panel BFFs that are compared to uPSP data.

D. Buffet Forcing Functions

In this section, a posteriori validation of the Corcos-based coherence factors is performed by comparing estimated panel BFFs based on the Corcos model to panel BFFs based on direct integration of uPSP data. First, the next subsection explains how to apply the Corcos-based coherence factors for BFF estimation. The subsequent two subsections provide detailed comparisons between modeled and benchmark BFFs for different Mach number and attitude conditions, and for different regions on the core stage.

1. Corcos-based BFF

The estimated Corcos BFF is computed as:

$$F_z(t) = \mathcal{F}^{-1}(\zeta(\omega)\widetilde{F}_z(\omega)) \tag{16}$$

where $\widetilde{F}_z(\omega) = C_p(\omega)\, Q\, A_z$ and $\mathcal{F}^{-1}$ represents an inverse Fourier transform from the frequency to the time domain. Thus, the Corcos-based coherence factor $\zeta(\omega)$ is utilized to attenuate the frequency content of a fully-coherent BFF defined by $\widetilde{F}_z(\omega)$. Two aspects are worth highlighting: 1) the Corcos-based coherence factor is frequency dependent, unlike other BFF integration methods (see Ref.[2]) that estimate coherence lengths based on an average coherence across the buffet frequency range. Ongoing studies (Refs.[16],[5]) indicate that frequency-dependent coherence factors yield more accurate BFF estimations than legacy methods. 2) In Eq. 16, an implicit assumption is that the estimated $F_z(t)$ shares the same phase as the fully-coherent force $\widetilde{F}_z(t)$.

The procedure for implementing Eq. 16 is as follows. The Fourier transform $\widetilde{F}_z(\omega) = \mathcal{F}(F_z(t))$ is computed using the FFT over the frequency interval $\omega \in 2\pi[0, F_s - F_s/N]$, where F_s is the sampling rate, N is the number of samples, and F_s/N is the frequency resolution. Note that the coherence factor $\zeta(\omega)$ was defined within the range $\omega \in [\omega_1, 2\pi\, F_s/2]$, where ω_1 is the lower bound of the low-frequency bin (see Fig. 4), and $F_s/2$ is the Nyquist frequency. To compute the product in Eq. 16, the definition of $\zeta(\omega)$ is extended as follows:

- for $\omega \in [0, \omega_1)$: $\zeta(\omega) = 1$.
- for $\omega \in [\omega_1, 2\pi\, F_s/2]$: $\zeta(\omega)$ is computed as described in Section II.C.1. As an example of the results, see Fig.13 (red-solid curve).
- for $\omega \in 2\pi(F_s/2, F_s - F_s/N]$: $\zeta(\omega) = 1$.

In computing the inverse Fourier transform (Eq. 16), it is assumed that the function $\zeta(\omega)\widetilde{F}_z(\omega)$ is conjugate symmetric (see MATLAB™ documentation for the IFFT function), and as a result, $F_z(t)$ is a real function.

2. Panel BFF validation

Figure 15 compares PSDs of F_z for panel #2 (Fig. 2), Φ_z^F, estimated using the Corcos model and direct integration of uPSP data. These PSDs are presented for three Mach numbers, Mach=0.79, 0.91, and 0.95, corresponding to coherence factors in Figs. 13 and 14. In Fig. 15, the black-dashed curves represent PSDs of the fully-coherent BFFs,

$\widetilde{F}_z(\omega) = C_p(\omega)\, Q\, A_z$, which, as expected, are an over-conservative estimate of the benchmark F_z, shown in green. The blue curves represent Φ_z^F estimated using the longitudinal, Corcos-based coherence factor alone, $\zeta_1(\omega)$, from Eq. 14. The red curves represent Φ_z^F estimated using $\zeta(\omega)$, based on Eq. 13, which accounts for both longitudinal and azimuthal coherence.

Compared to the fully-coherent BFFs (black-dashed curve in Fig. 15), the Corcos-based BFFs provide a closer approximation of the benchmark, although the Mach=0.91, Corcos-based BFFs are over-conservative for reasons discussed in the next paragraph. Overall, the distributions of Φ_z^F based on $\zeta(\omega)$ bound the benchmark from above, while Φ_z^F based on the low-frequency bin $\zeta_1(\omega)$ is slightly underconservative for the Mach=0.95 case. Note that for visualization purposes, the blue and red curves are broken into three sets corresponding to low-, mid-, and high-frequency bins while Φ_z^F is actually a continuous function. At the boundaries between these frequency bins, the slope of Φ_z^F is irregular due to discontinuities of the coherence factors across those boundaries (Fig.13). One method to smooth out the slope of Φ_z^F is to interpolate the coherence factors. Figures 13 and 14 show 5th-order polynomial interpolations of $\zeta(\omega)$ (red-dashed curves) fairing through distributions of $\zeta(\omega)$ across frequency bins. Power spectral densities of BFFs employing interpolated coherence factors are shown in Fig. 16.

The Corcos-based BFFs at Mach=0.91 (Fig. 15-b) are overconservative relative to direct uPSP integration, especially in the midfrequency range. Two factors contribute to this overconservatism. First, in this frequency range $\zeta = 1$ (Fig. 14-a), due to highly-coherent pressure fluctuations associated with FAH vortex-shedding, thus no attenuation takes place. Second, at Mach=0.91, pressure fluctuations within panel #2 boundaries are spatially nonuniform, compared to other Mach conditions. Figure 17 compares distributions of uPSP-based $C_{p,\mathrm{rms}}$ for Mach=0.79, 0.91, and 0.95 on the core stage. Data are unwrapped between ±1 core diameters from the reference supernode and $\Delta\theta \in [0 - 360]$ deg., where θ is a body coordinate system azimuthal angle, and $\Delta\theta = 0$ through the reference supernode. Gray areas that lack $C_{p,\mathrm{rms}}$ data could not be imaged by uPSP cameras due to presence of the boosters and limitations of camera fields of view. Comparing Mach=0.79 and Mach=0.91 (Fig. 17-a,b), at Mach=0.91, $C_{p,\mathrm{rms}}$ varies significantly within panel #2. This variation contributes to lower the magnitude of $|H(\omega)| = |F_z(\omega)/\widetilde{F}_z(\omega)|$, compare the green curves of Fig. 13 and Fig. 14-a. It is important to stress that nonuniform fluctuating-pressure environments pose a challenge to any BFF estimation method that is based on discrete experimental measurements from rigid buffet models, such as the Corcos-based method. In such environments, the precise location of the pressure measurement can lead to over- or underestimation of the BFFs. For example, Ref.[16] discusses a buffet integration region that contains a terminal shock. Buffet Forcing Functions estimated from discrete pressure measurements taken within that region are very sensitive to the freestream Mach number and the longitudinal location of the pressure sensor.

At Mach=0.95, panel #2 is located in a relatively low $C_{p,\mathrm{rms}}$ region and spatially uniform environment, as highlighted by the $C_{p,\mathrm{rms}}$ contours of Fig. 17-c. In this environment, that is presumably dominated by turbulent boundary layer fluctuations, the Corcos-based Φ_z^F are in very good agreement with the benchmark (Fig. 15-c). On the leeward side, where high pressure fluctuations are dominated by FAH vortex-shedding (Fig. 17-c), the Corcos-based BFFs are overly conservative relative to direct integration of uPSP data (not shown). This conservatism is, again, due to vortex-shedding-induced spatial nonuniformity within the integration boundaries.

3. Buffet environments on other regions of the vehicle

Figure 18 extends comparisons of Φ_z^F between Corcos-based BFFs and direct integration of uPSP data to panels located downstream of the FAH. The location of these panels is illustrated in Fig. 2. The Mach number is 0.79 and the vehicle is at zero degrees attitude. Agreement between the Corcos-based BFFs and the benchmark is satisfactory. For panels closer to the FAH, e.g., #1 through #8, the Corcos-based BFFs are more conservative relative to the benchmark than for downstream panels #9 through #16. This difference in conservatism is because downstream of the FAH the impact of TBL on pressure fluctuations strengthens relative to vortex shedding, thus the Corcos model performs better.

III. Conclusions

In this paper, a methodology was developed for validation and application of the Corcos model to the modeling of transonic buffet environments of launch vehicles. This study was made possible by a unique data set comprised of high-spatial-resolution unsteady Pressure Sensitive Paint (uPSP) measurements collected on a Space Launch System configuration. The analysis focuses on the core stage region located downstream of the forward attachment hardware between the core and solid rocket boosters. In this region, the vehicle experiences peak fluctuating forces due to vortex shedding off the attachment hardware. As a general conclusion, the Corcos-based coherence function, and its

derived quantities, including buffet forcing functions (BFFs), performed reasonably well in regions of the vehicle and frequency bands where pressure fluctuations are mostly associated with turbulent boundary layer (TBL). Non-TBL related environments, such as vortex shedding, or spurious tunnel tones, caused deviations between the Corcos model and uPSP data.

The Corcos model similarity and multiplication hypotheses were tested. Invoking the first hypothesis, a reasonable collapse of the longitudinal (i.e., streamwise) and azimuthal (i.e., crossflow) coherence function distributions was found within a typical bandwidth associated with transonic buffet. Dividing up the buffet bandwidth into low-, mid-, high-frequency bins improved self-similarity of the coherence function within each bin. Certain phenomena contributed to deviations from predictions by the Corcos model. Mainly, at lower Mach numbers (Mach=0.79), the coherence function has a pronounced oscillatory behavior (traces of which are seen also at higher Mach conditions), especially in the midfrequency range. It was demonstrated that this behavior can be captured by a modified version of the Corcos-based longitudinal coherence function. Also in the midfrequency range, vortex shedding off the forward attachment hardware is a major source of pressure fluctuations and associated coherence, especially near Mach=0.91.

Analysis of the Corcos decay constants revealed that the streamwise parameter is much higher than typical Corcos values (0.11-0.12), especially at low frequencies, while the crossflow parameter is closer to typical values (0.7-1.2), in the mid- and high- frequency range. Notably, for the Mach numbers analyzed, local minima and inflections of the Corcos parameters are found near Mach=0.91. The multiplication hypothesis was also tested, indicating a general agreement between the Corcos model and uPSP data.

Coherence lengths estimated based on the Corcos model follow a ω^{-1} trend and provide a reasonable approximation of those directly computed from uPSP data, used as benchmark values. However, trends of uPSP-based coherence lengths are nonmonotonic, due to the impact that vortex shedding has on the coherence function as well as spurious tunnel tones. Utilizing the modeled coherence lengths, a set of longitudinal and azimuthal coherence factors were computed for sample panels on the core stage. Based on the proposed definitions, these coherence factors follow trends that are either constant (equal to 1) or decay as a function of $\omega^{-0.5}$. A combined coherence factor was also defined, as an average between longitudinal and azimuthal coherence factors. This combined coherence factor was found to be a best compromise for BFF estimation. In contrast, coherence factors that follow a $\omega^{-1.0}$ trend, such as, e.g., those based on the product $\zeta_1\zeta_3$, lead to underconservative BFF estimates relative to uPSP data. Trends of longitudinal, azimuthal and average coherence factors with frequency are consistent with those of a high-fidelity frequency response function (H) based on uPSP data. However, by definition, the Corcos-based coherence factors are constrained to negative-slope linear functions on a logarithmic scale, whereas the slope of H varies continuously on the same logarithmic scale.

Power spectral densities of BFFs estimated using the Corcos-based coherence factors are in good agreement with direct integration of uPSP data, except under conditions where pressure fluctuations within the integration boundaries are spatially nonuniform. This nonuniformity was most pronounced for panels located along the trajectory of shed vortices from the forward attachment hardware. The strength and trajectory of these vortices vary with the attitude of the vehicle, as well as Mach numbers, with the Mach=0.91-0.95 range showing peak pressure fluctuations. Under these conditions, coherence factors overestimate H and, as a result, the Corcos-based BFFs overpredict the benchmark. These deficiencies of modeled BFFs in regions of pressure nonuniformity are an inherent limitation of discrete-measurement-based BFF estimation methods, rather than the Corcos model.

Acknowledgment

The authors would like to thank the uPSP test team at the NASA Ames Research Center, to include Nettie Roozeboom, Jennifer Baerny, Jie Li, David Murakami, Marc Shaw-Lecerf, Paul Stremel, and Lucy Tang and also Jessica Powell at the NASA Johnson Space Center for their invaluable assistance in acquiring, processing, and discussing the uPSP data analyzed in this paper. Also, the authors would like to thank Craig Streett of the NASA Langley Research Center for reviewing the paper and for his helpful comments.

References

[1] NASA, "NASA-STD-5002A: Load Analyses of Spacecraft and Payloads," Tech. rep., NASA, 2019.

[2] Piatak, D. J., Sekula, M. K., and Rausch, R. D., "Ares Launch Vehicle Transonic Buffet Testing and Analysis Techniques," *Journal of Spacecraft and Rockets*, Vol. 49, No. 5, 2012, pp. 798–807. doi:10.2514/1.A32175, URL `https://doi.org/10.2514/1.A32175`.

[3] Sekula, M. K., Piatak, D. J., and Rausch, R., *Effect of Surface Pressure Integration Methodology on Launch Vehicle Buffet Forcing Functions*, 2016. doi:10.2514/6.2016-0545, URL https://arc.aiaa.org/doi/abs/10.2514/6.2016-0545.

[4] Panda, J., "Experimental Verification of Buffet Calculation Procedure Using Unsteady Pressure-Sensitive Paint," *Journal of Aircraft*, Vol. 54, No. 5, 2017, pp. 1791–1801. doi:10.2514/1.C033917, URL https://doi.org/10.2514/1.C033917.

[5] Ramey, J. M., Sekula, M. K., Piatak, D. J., Heaney, P. S., and Soranna, F., "Development of Buffet Forcing Functions using Frequency-Dependent Coherence Factors," *AIAA SciTech 2021 Forum*, 2021.

[6] Corcos, G. M., "Resolution of Pressure in Turbulence," *Acoustical Society of America Journal*, Vol. 35, No. 2, 1963, p. 192. doi:10.1121/1.1918431.

[7] Roozeboom, N., Powell, J., Baerny, J., Murakami, D., Ngo, C., Garbeff, T. J., Ross, J. C., and Flach, R., *Development of Unsteady Pressure-Sensitive Paint Application on NASA Space Launch System*, 2019. doi:10.2514/6.2019-3502, URL https://arc.aiaa.org/doi/abs/10.2514/6.2019-3502.

[8] Soranna, F., Sekula, M. K., Heaney, P. S., Ramey, J. M., and Piatak, D. J., *Coherence Analysis of the Space Launch System using Unsteady Pressure Sensitive Paint*, 2021. doi:10.2514/6.2021-1834, URL https://arc.aiaa.org/doi/abs/10.2514/6.2021-1834.

[9] Hwang, Y. F., and Maidanik, G., "A wavenumber domain analysis of the coupling of a structural mode and flow turbulence," *The Journal of the Acoustical Society of America*, Vol. 84, No. S1, 1988, pp. S88–S88. doi:10.1121/1.2026535, URL https://doi.org/10.1121/1.2026535.

[10] Singer, B. A., "Turbulent Wall-Pressure Fluctuations: A New Model for Off-Axis Cross-Spectral Density," *J. Fluids Eng.*, Vol. 119, No. 2, 1997, pp. 277–280.

[11] Di Marco, A., Camussi, R., Bernardini, M., and Pirozzoli, S., "Wall pressure coherence in supersonic turbulent boundary layers," *Journal of Fluid Mechanics*, Vol. 732, 2013, p. 445–456. doi:10.1017/jfm.2013.410.

[12] Bremner, P., Blelloch, P., Hutchings, A., Shah, P., Streett, C., and Larsen, C., *Validation of Methods to Predict Vibration of a Panel in the Near Field of a Hot Supersonic Rocket Plume*, 2011. doi:10.2514/6.2011-2852, URL https://arc.aiaa.org/doi/abs/10.2514/6.2011-2852.

[13] Pröbsting, S., Scarano, F., Bernardini, M., and Pirozzoli, S., "On the estimation of wall pressure coherence using time-resolved tomographic PIV," *Experiments in Fluids*, Vol. 54, No. 7, 2013, p. 1567. URL https://doi.org/10.1007/s00348-013-1567-6.

[14] Palumbo, D., "Determining correlation and coherence lengths in turbulent boundary layer flight data," *Journal of Sound and Vibration*, Vol. 331, No. 16, 2012, pp. 3721 – 3737. doi:https://doi.org/10.1016/j.jsv.2012.03.015, URL http://www.sciencedirect.com/science/article/pii/S0022460X12002106.

[15] Dahm, W. K., "Composite Model of a Random Forcing Function for the Excitation of a Long Pipes by a Cross Flow," NASA Marshall Space Flight Center Memo ED31-79-15, Aug. 1979.

[16] Soranna, F., Heaney, P. S., Sekula, M. K., Piatak, D. J., Ramey, J. M., Roozeboom, N. H., Murakami, D. D., Baerny, J. K., Stremel, P. M., Jessica, J. L., and Powell, M., "Analysis of Buffet Forcing Functions Estimated from Unsteady Pressure Sensitive Paint," *AIAA Aviation 2020 Forum*, 2020.

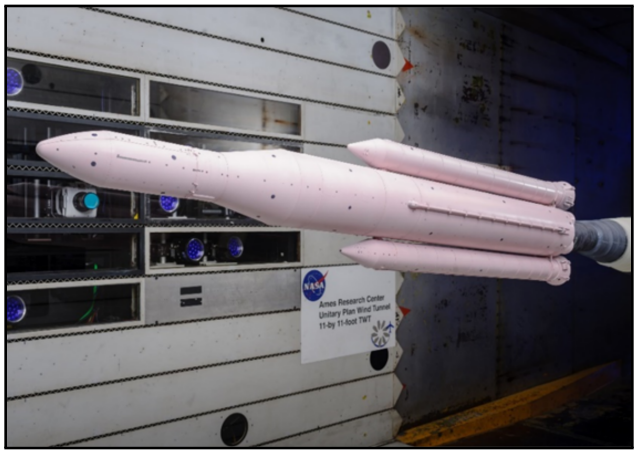


Fig. 1 SLS Block 1 cargo 2.5-percent scale model tested during ATAT.

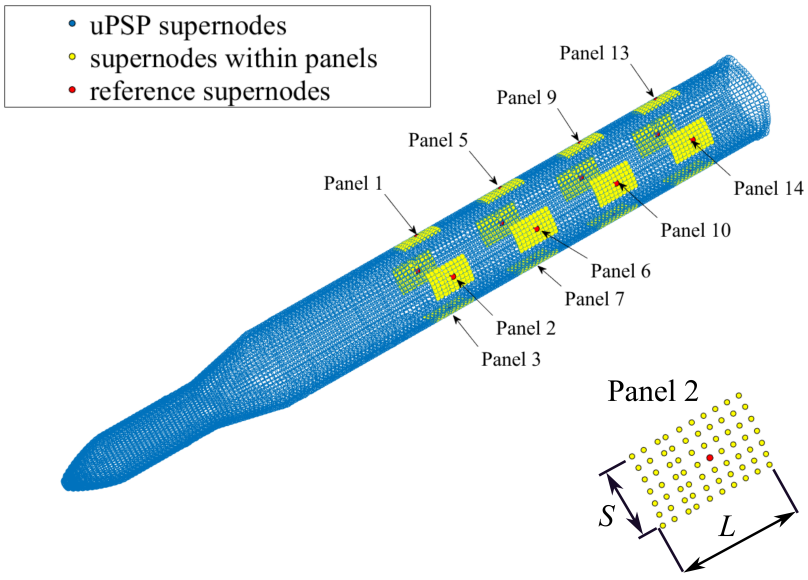


Fig. 2 uPSP supernodes for the SLS Block 1 cargo core stage. Also shown are panels for BFF analysis (regions marked in yellow) and characteristic dimensions for a reference panel (bottom right inset).

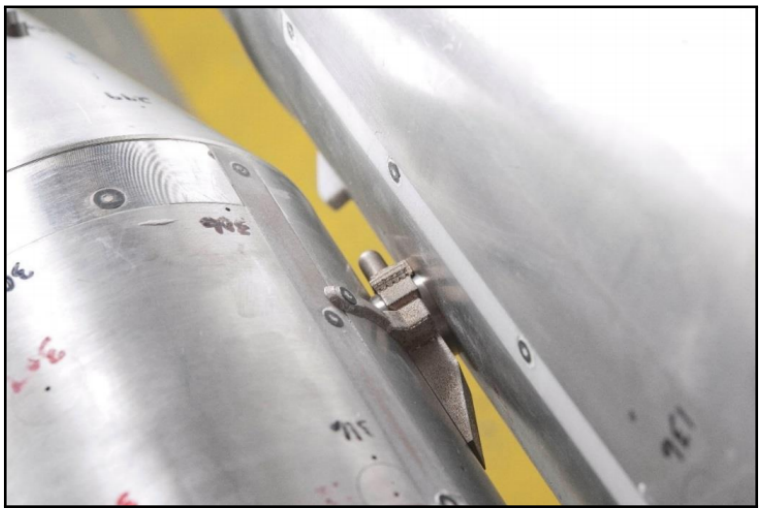


Fig. 3 SLS Booster forward attachment hardware.

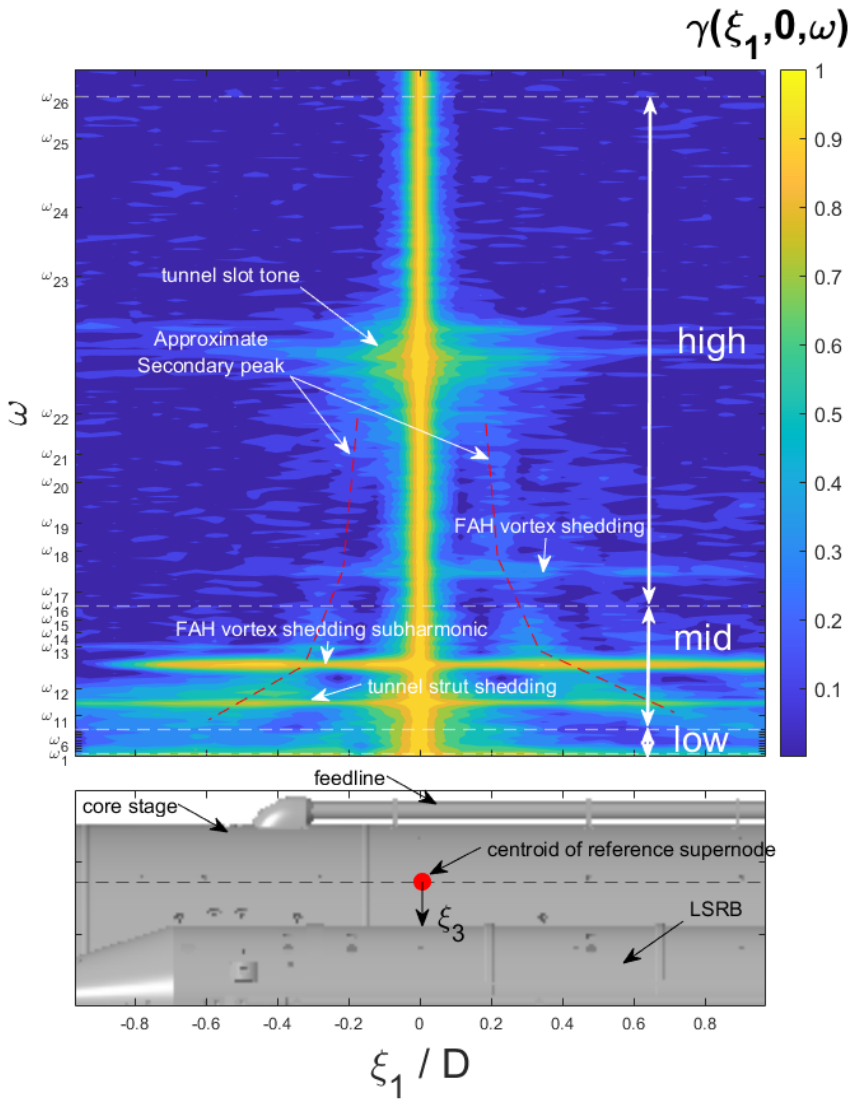
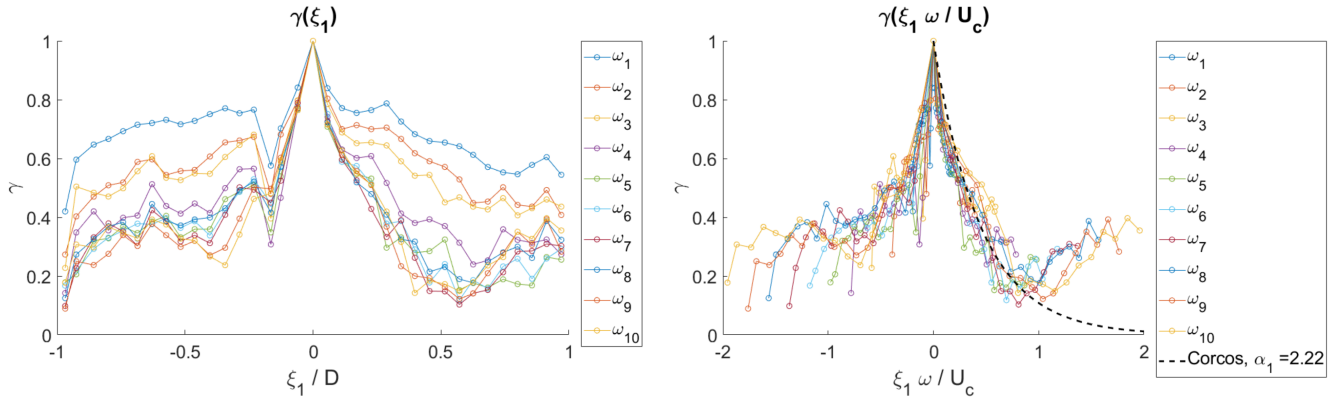
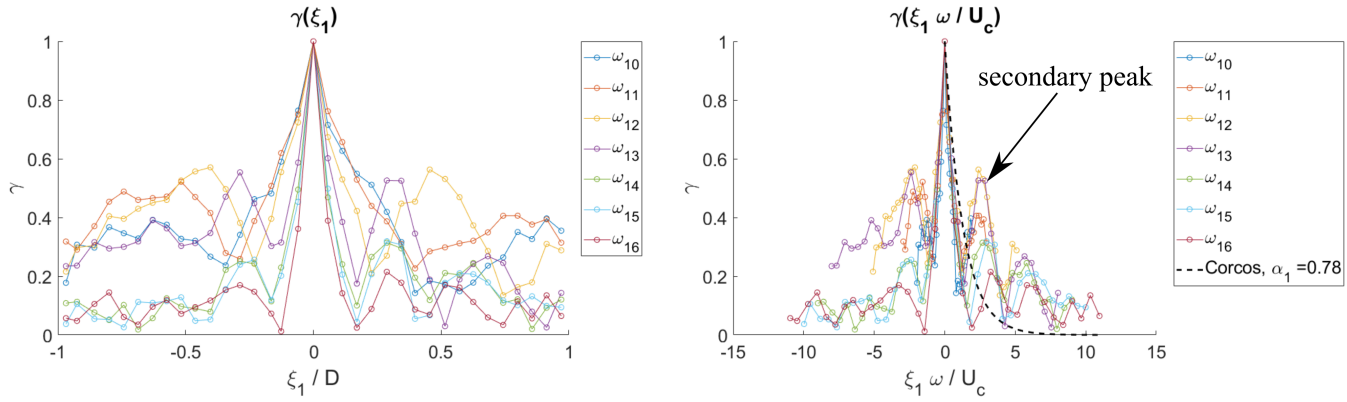


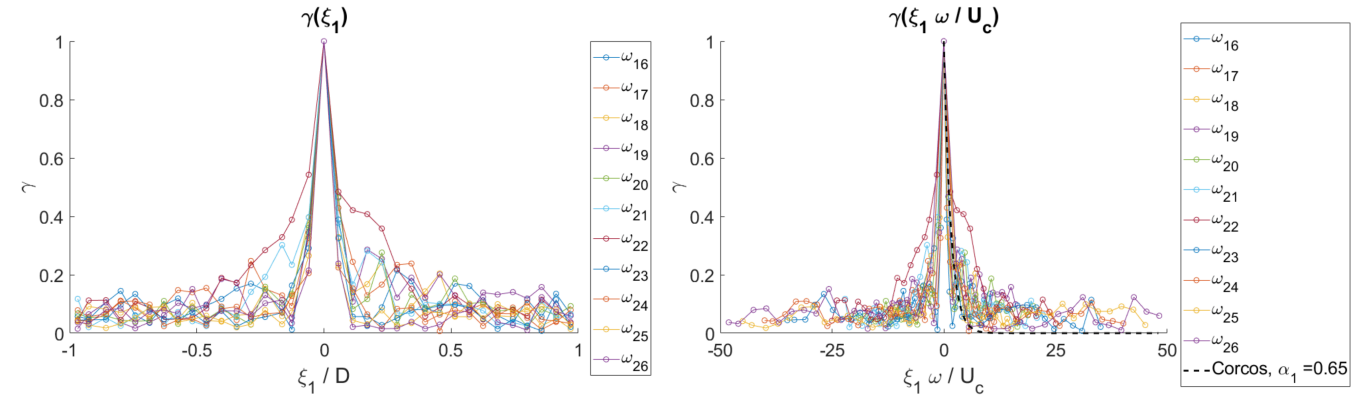
Fig. 4 Contours of the streamwise (longitudinal) coherence function, $\gamma(\xi_1, 0, \omega)$, on a θ = constant plane for a reference supernode on the Block 1 cargo core stage. Also shown, the OML of the vehicle (bottom) and the longitudinal segment (dashed line) on the OML where the γ-distribution is taken. Mach = 0.79, $\alpha = 0$ deg, and $\beta = 0$ deg.



(a) low-frequency range



(b) midfrequency range



(c) high-frequency range

Fig. 5 ω **= constant slices of the contour plot of Fig. 4. Left column: distributions of** $\gamma(\xi_1)$**. Right column: distributions of** $\gamma(\xi_1\omega/U_c)$**. Dashed curve: Corcos exponential function** $A(\omega\xi_1/U_c)$ **(Eq. 2). Mach = 0.79,** $\alpha = 0$ **deg, and** $\beta = 0$ **deg.**

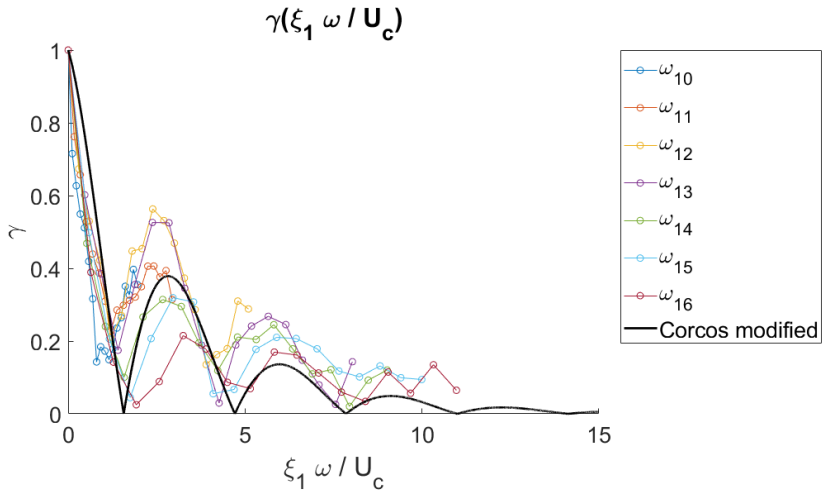


Fig. 6 Distributions of $\gamma(\xi_1\omega/U_c)$ for the midfrequency range (from Fig. 5-b, right column) compared to the Corcos modified coherence function (black line) from Eq. 7). Mach = 0.79, $\alpha = 0$ deg, and $\beta = 0$ deg.

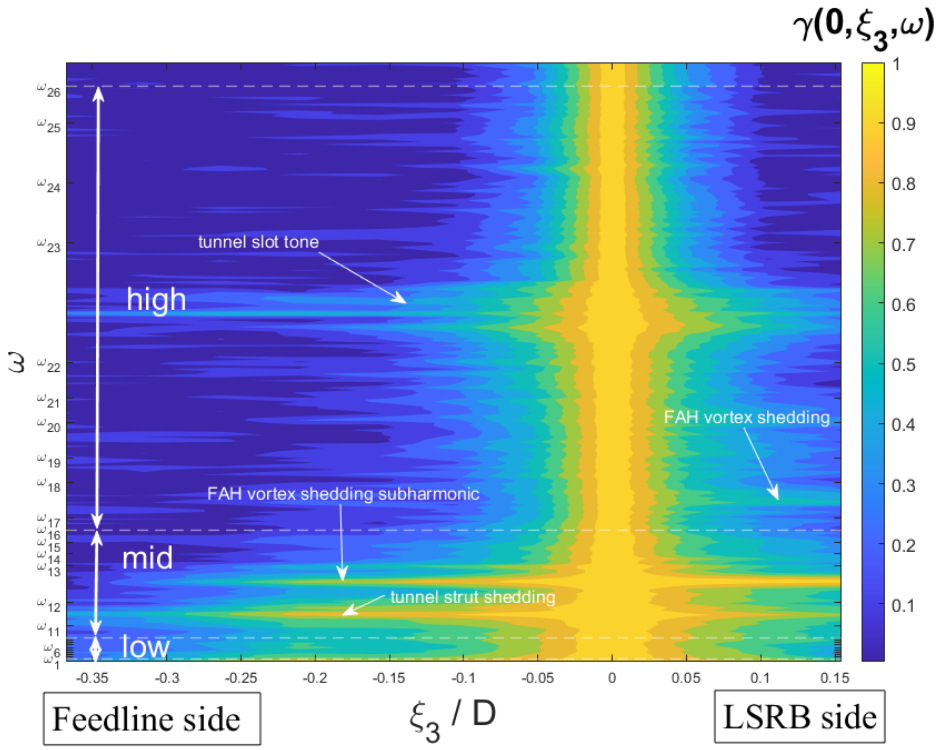
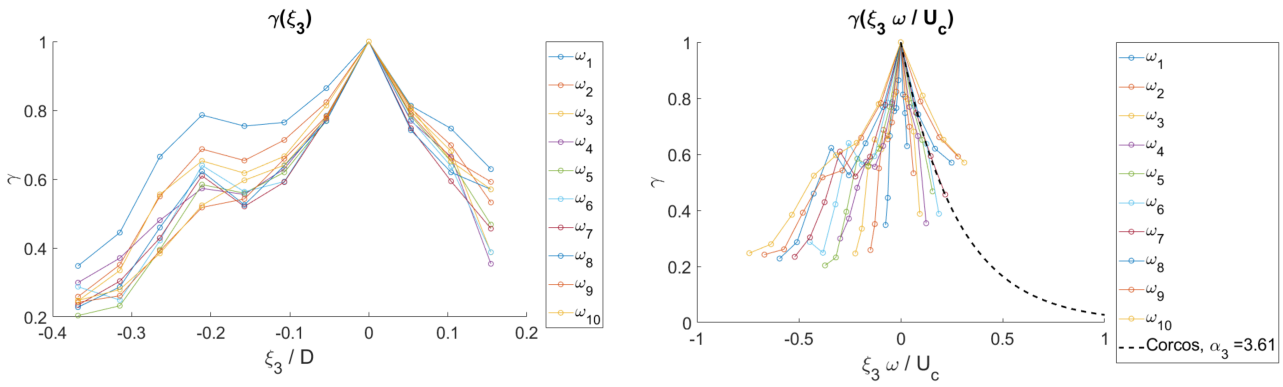
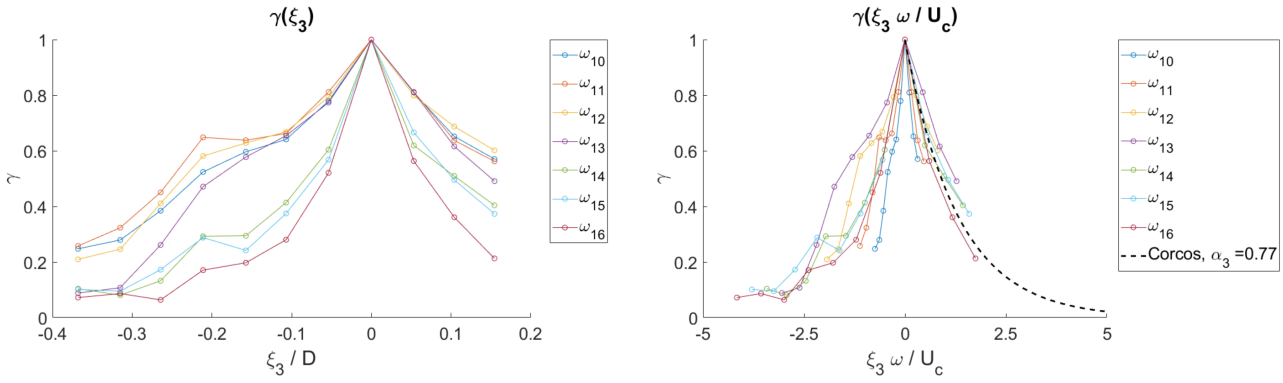


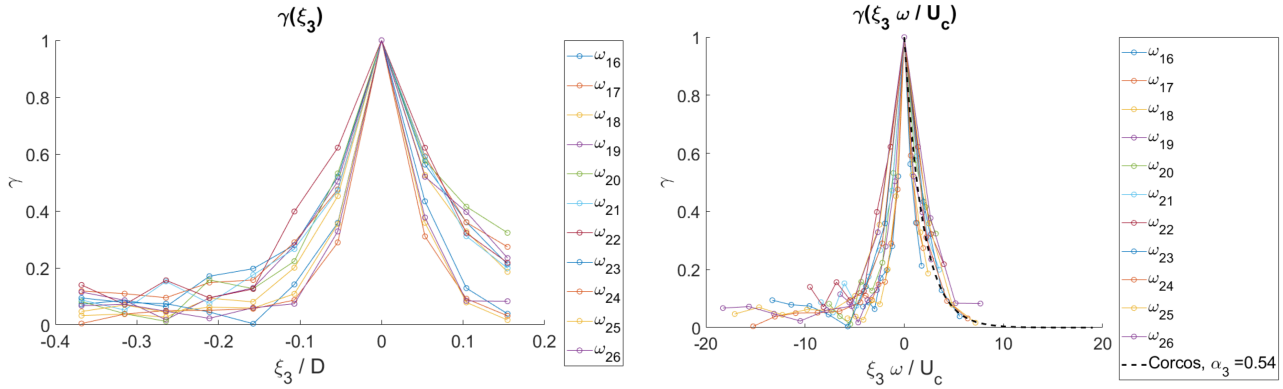
Fig. 7 Contours of the crossflow (azimuthal) coherence function, $\gamma(0, \xi_3, \omega)$, on a x = constant plane for a reference supernode shown in Fig. 4. Mach = 0.79, $\alpha = 0$ deg, and $\beta = 0$ deg.



(a) low-frequency range

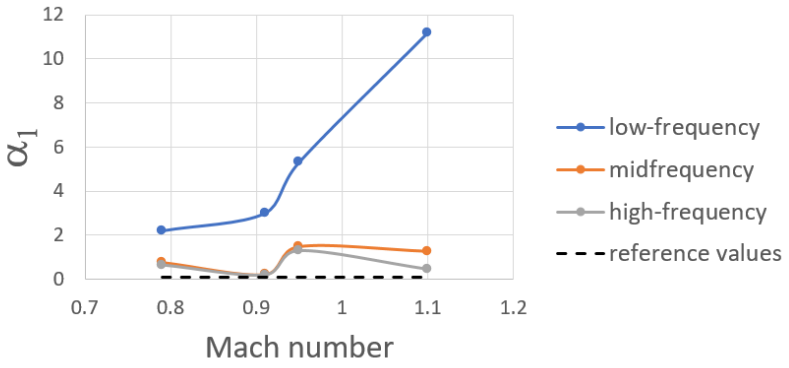


(b) midfrequency range

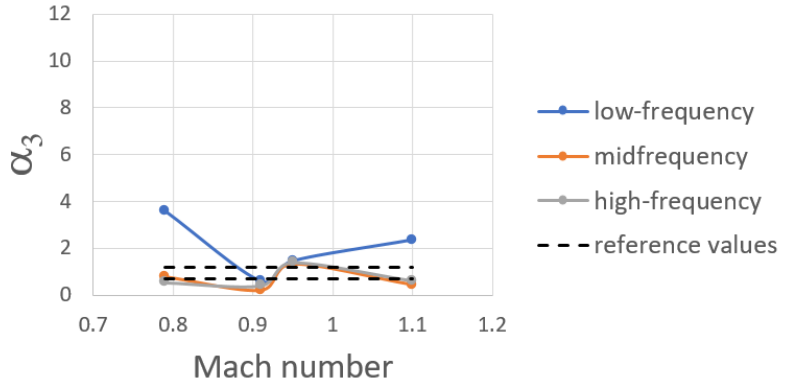


(c) high-frequency range

Fig. 8 ω **= constant slices of the contour plot of Fig. 7. Left column: distributions of** $\gamma(\xi_3)$**. Right column: distributions of** $\gamma(\xi_3\omega/U_c)$**. Dashed curve: Corcos exponential function** $B(\omega\xi_3/U_c)$ **(Eq. 2). Mach = 0.79,** $\alpha = 0$ **deg, and** $\beta = 0$ **deg.**

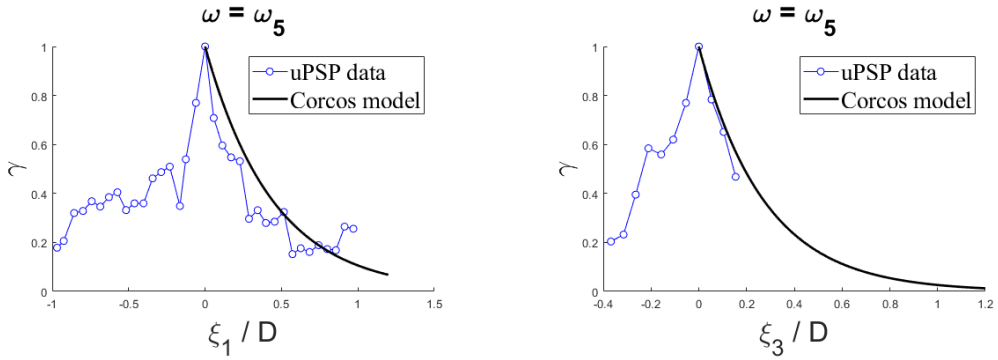


(a)



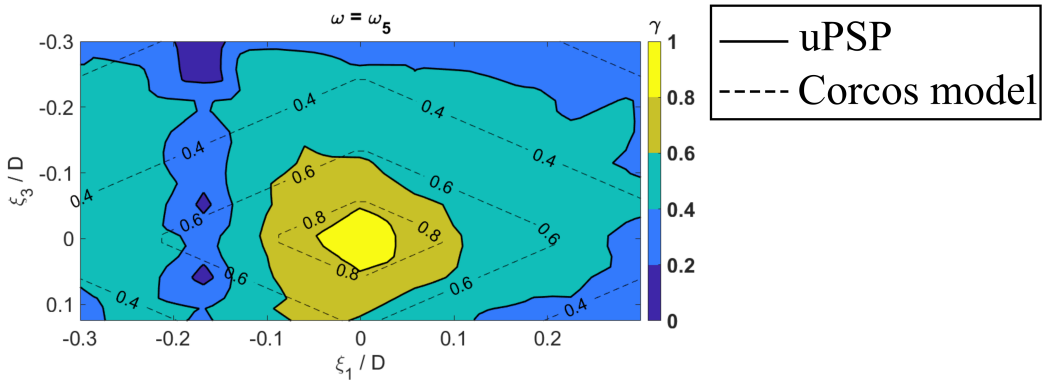
(b)

Fig. 9 Distributions of Corcos decay constants (a) α_1 and (b) α_3 as a function of Mach number (Table 1) for the reference supernode of Fig. 4.

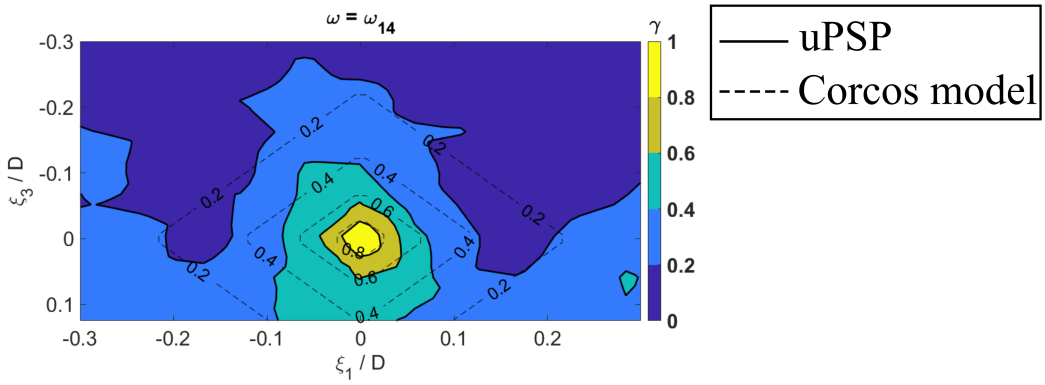


(a) $\gamma(\xi_1)$ **(b)** $\gamma(\xi_3)$

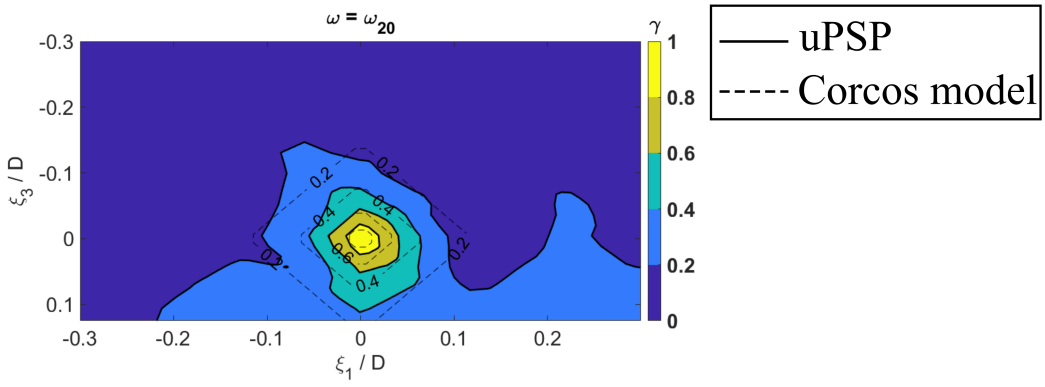
Fig. 10 Distributions of (a) $\gamma(\xi_1)$ and (b) $\gamma(\xi_3)$ for the reference supernode of Fig. 4 and a sample ω within the low-frequency range ($\omega = \omega_5$, see ω_i labels in Fig. 4). Mach = 0.79, $\alpha = 0$ deg, and $\beta = 0$ deg.



(a) low-frequency sample

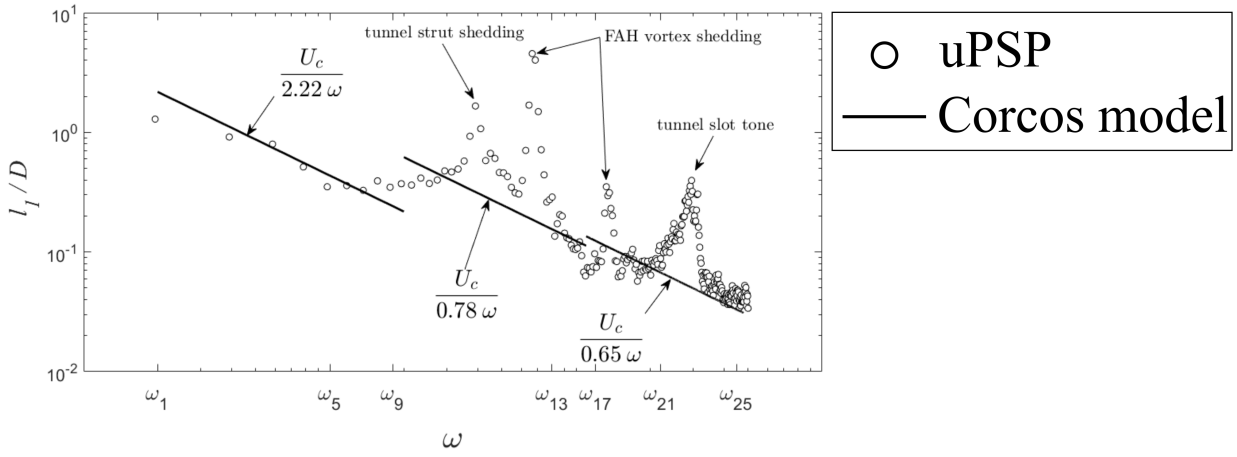


(b) midfrequency sample

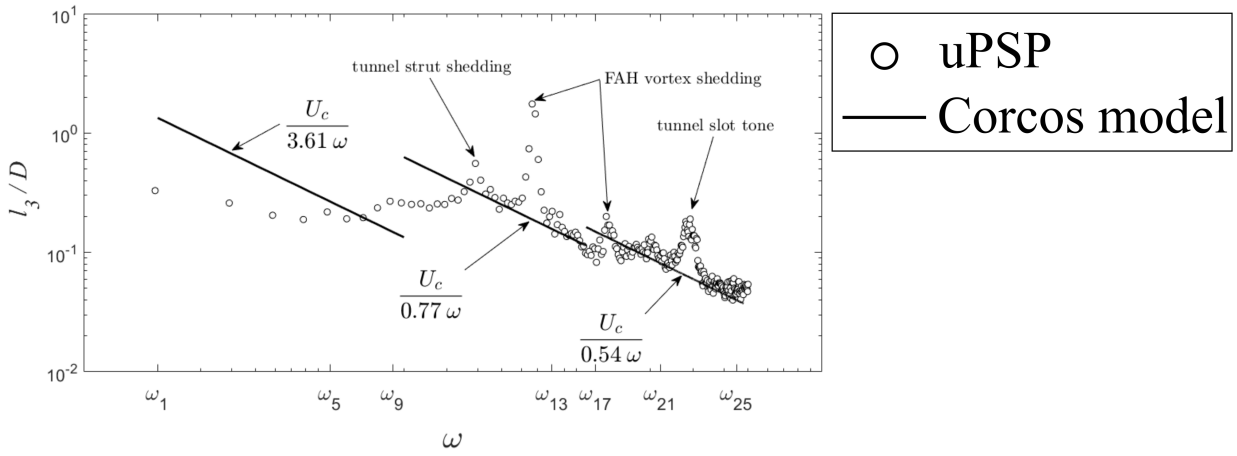


(c) high-frequency sample

Fig. 11 Distributions of $\gamma(\xi_1, \xi_3)$ for the reference supernode of Fig. 4 and sample low- (a), mid- (b), and high- (c) frequencies ω_i (see ω_i labels in Fig. 4). Mach = 0.79, $\alpha = 0$ deg, and $\beta = 0$ deg.



(a)



(b)

Fig. 12 Distributions of (a) streamwise (l_1) and (b) crossflow (l_3) coherence lengths as a function of frequency for the reference supernode of Fig. 4. Mach = 0.79, $\alpha = 0$ deg, and $\beta = 0$ deg.

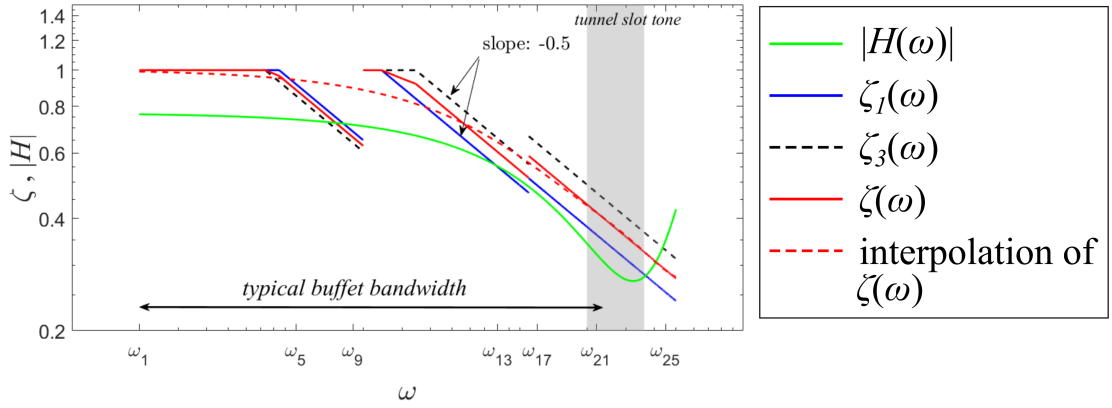
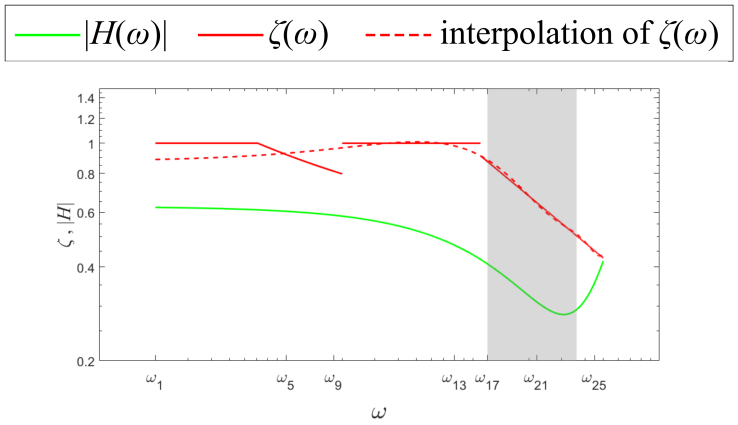
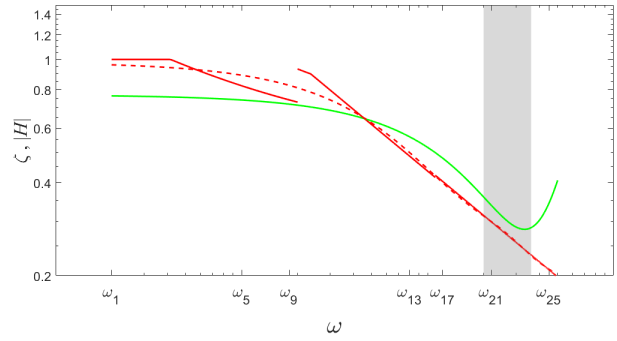


Fig. 13 Comparison of panel BFF coherence factors based on the Corcos model to uPSP-based frequency response function $H(\omega)$, for panel #2 shown in Fig. 2. Mach = 0.79, $\alpha = 0$ deg, and $\beta = 0$ deg.

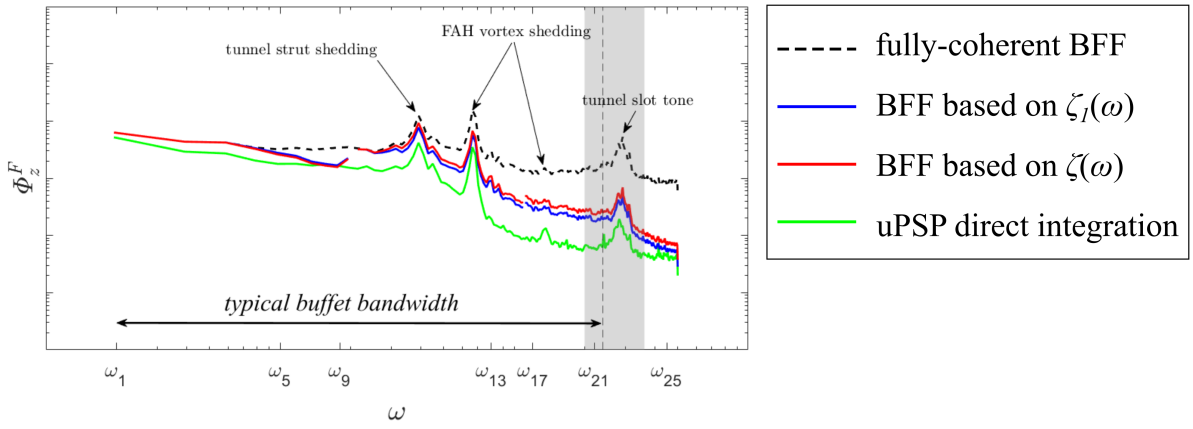


(a) Mach = 0.91, $\alpha = 0$ deg, and $\beta = 0$ deg.

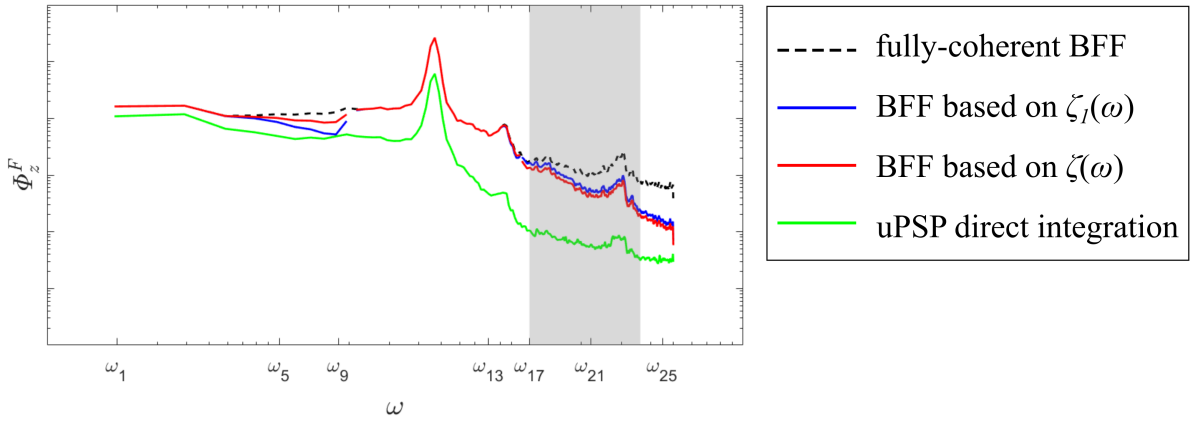


(b) Mach = 0.95, $\alpha = -4.0$ deg, and $\beta = 0$ deg.

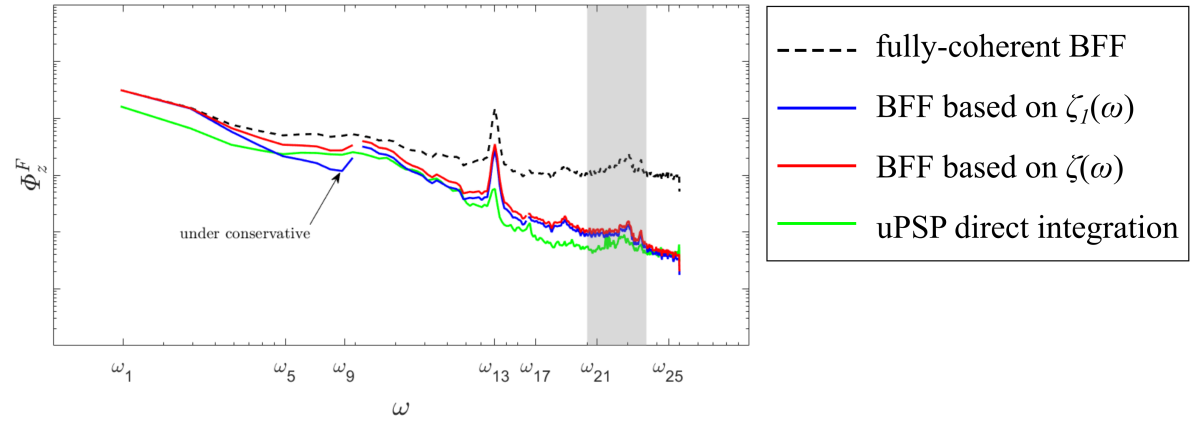
Fig. 14 Comparison of panel BFF coherence factors based on the Corcos model to uPSP-based frequency response function $H(\omega)$, for panel #2 shown in Fig. 2. Shaded: tunnel slot tone.



(a) Mach = 0.79, $\alpha = 0$ deg, and $\beta = 0$ deg.



(b) Mach = 0.91, $\alpha = 0$ deg, and $\beta = 0$ deg.



(c) Mach = 0.95, $\alpha = -4.0$ deg, and $\beta = 0$ deg.

Fig. 15 Comparison of Φ_z^F for panel #2 shown in Fig. 2.

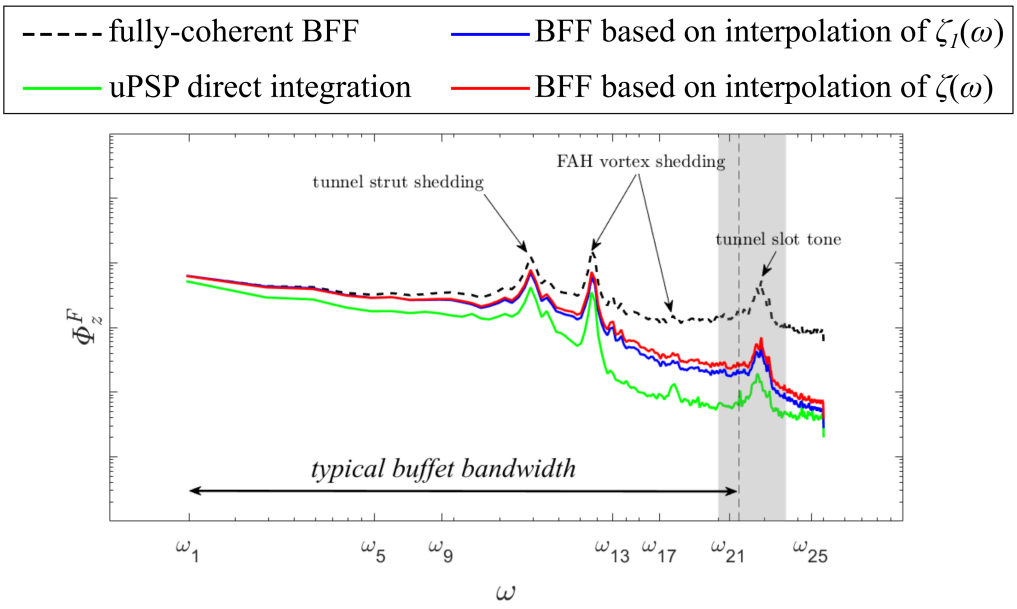


Fig. 16 Distributions of Φ_z^F for panel #2 (Fig. 2) after interpolation of coherence factors of Fig. 13. Mach = 0.79, $\alpha = 0$ deg, and $\beta = 0$ deg.

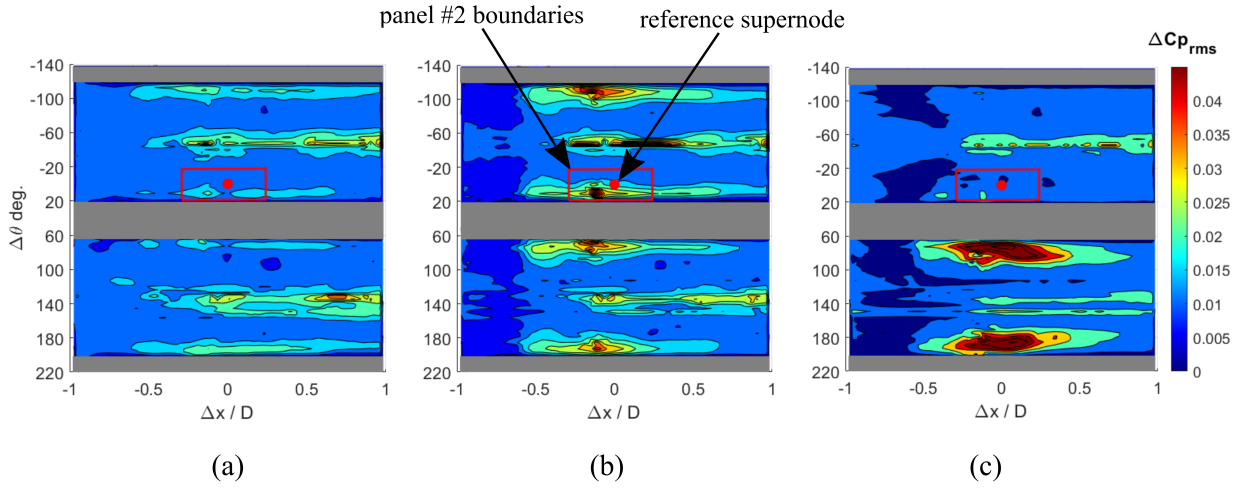


Fig. 17 Comparison of $\Delta C_{p,\mathrm{rms}}$ on the core stage. Shaded: SRB's blockage. (a) Mach = 0.79, $\alpha = 0$ deg, and $\beta = 0$ deg, (b) Mach = 0.91, $\alpha = 0$ deg, and $\beta = 0$ deg, and (c) Mach = 0.95, $\alpha = -4.0$ deg, and $\beta = 0$ deg.

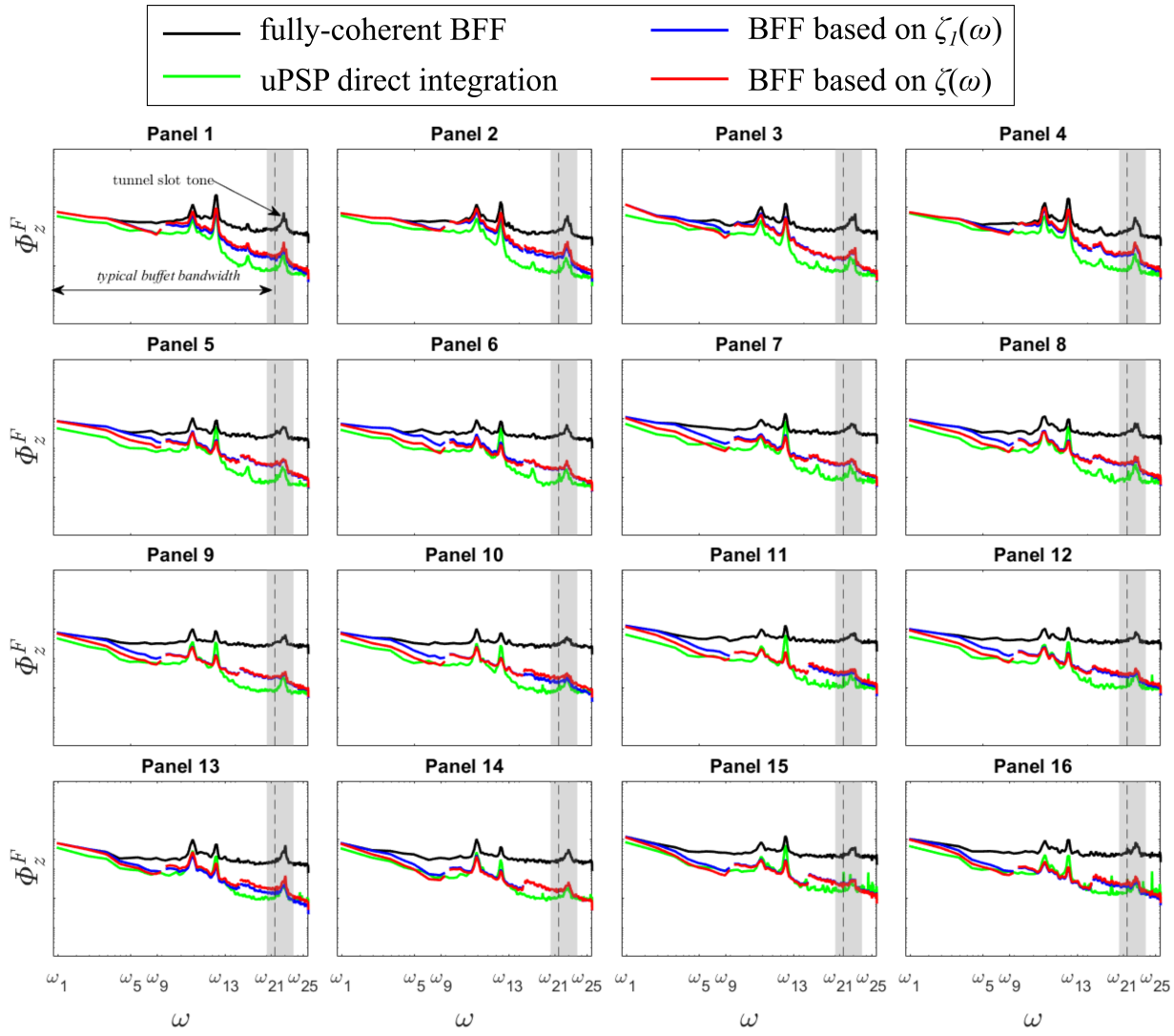


Fig. 18 Comparison of Φ_z^F for the panels shown in Fig. 2. Mach = 0.79, $\alpha = 0$ deg, and $\beta = 0$ deg.